EUROPEAN ORGANIZATION FOR NUCLEAR RESEARCH (CERN)

CERN-EP-2022-177
2022/11/29

CMS-SMP-21-014
TOTEM NOTE 2022-004

Search for high-mass exclusive $\gamma\gamma \to \mathrm{WW}$ and $\gamma\gamma \to \mathrm{ZZ}$ production in proton-proton collisions at $\sqrt{s} = 13\,\mathrm{TeV}$

The CMS and TOTEM Collaborations

Abstract

A search is performed for exclusive high-mass $\gamma\gamma \to \mathrm{WW}$ and $\gamma\gamma \to \mathrm{ZZ}$ production in proton-proton collisions using intact forward protons reconstructed in near-beam detectors, with both weak bosons decaying into boosted and merged jets. The analysis is based on a sample of proton-proton collisions collected by the CMS and TOTEM experiments at $\sqrt{s} = 13\,\mathrm{TeV}$, corresponding to an integrated luminosity of $100\,\mathrm{fb}^{-1}$. No excess above the standard model background prediction is observed, and upper limits are set on the $\mathrm{pp} \to \mathrm{pWWp}$ and $\mathrm{pp} \to \mathrm{pZZp}$ cross sections in a fiducial region defined by the diboson invariant mass $m(\mathrm{VV}) > 1\,\mathrm{TeV}$ (with $\mathrm{V} = \mathrm{W}, \mathrm{Z}$) and proton fractional momentum loss $0.04 < \xi < 0.20$. The results are interpreted as new limits on dimension-6 and dimension-8 anomalous quartic gauge couplings.

Submitted to the Journal of High Energy Physics

1 Introduction

A class of proton-proton scattering events at the CERN LHC exists in which the incoming protons radiate high-energy quasireal photons and remain intact, whereas only the two photons interact, as shown in Fig. 1. The protons lose a small fraction of their initial 6.5 TeV energy and are scattered at very small angles. In the CMS experiment, the scattered protons are measured with the Precision Proton Spectrometer (PPS), a set of near-beam detectors located on both sides of the central elements of the CMS detector at around 200 m from the interaction point (IP) [1, 2]. The trajectories of the scattered protons are bent by the LHC magnets between the interaction point and the PPS detectors, which makes it possible to measure their momenta. By reconstructing both protons, the center-of-mass energy of the two-photon collision is determined on an event-by-event basis.

In the present paper, a search is presented for the exclusive production of gauge boson pairs (WW or ZZ) from $\gamma\gamma$ interactions using the PPS. The final state consists solely of the two bosons and the scattered protons, which are reconstructed using PPS. The fully hadronic decay modes of the W and Z bosons are studied. When the gauge bosons are produced with a large boost, as expected in many scenarios beyond the standard model (BSM), decay products of each of the bosons are merged into a single large-area jet.

The branching fraction of the fully hadronic channel for W and Z bosons is the highest (67–70%), but this mode is not accessible without the proton detection because of the very large background from jet production in quantum chromodynamics (QCD) processes. For exclusive production when the protons are measured, the kinematics of the final-state bosons can be independently reconstructed both with the central part of the CMS detector and with PPS. Therefore, for signal events that are correctly identified, the entire 13 TeV collision energy can be reconstructed in the four-body pWWp or pZZp system.

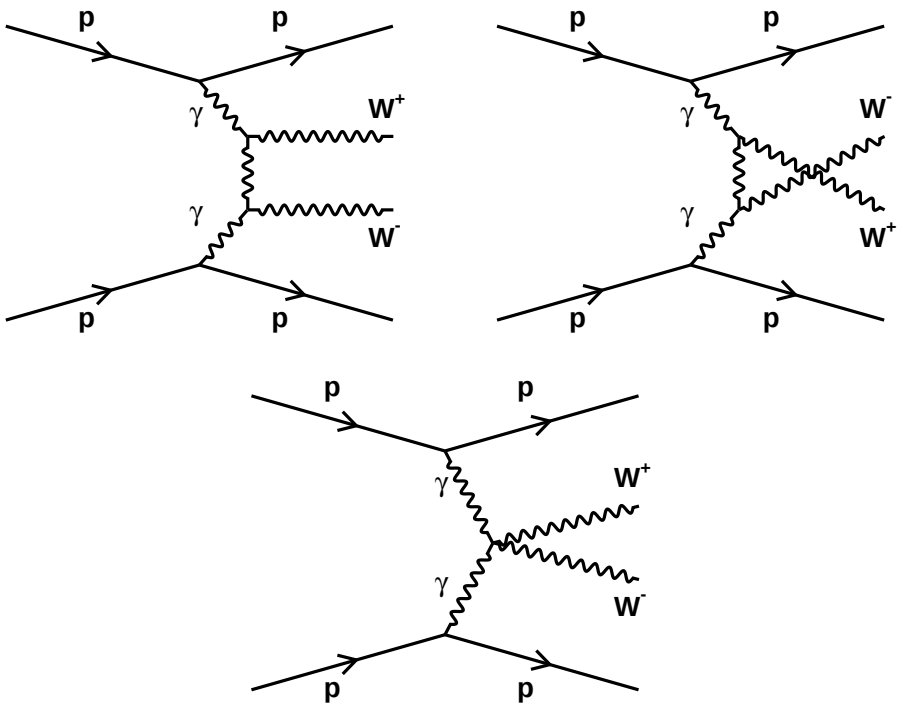

Figure 1: Schematic diagrams of exclusive $\gamma\gamma \to$ WW production with intact protons according to the standard model (SM).

Within the SM, quartic couplings involving two-photon production of charged ($W^{\pm}$) gauge bosons are allowed at tree level, as illustrated in Fig. 1. Because of gauge invariance, the strength of these couplings is related to the triple gauge couplings, which enter through t- and u-channel $\gamma\gamma \to WW$ production, and is fully specified in the SM. The SM cross sections for the $\gamma\gamma \to WW$ and $\gamma\gamma \to ZZ$ processes with both protons intact are expected to be around 50 fb and 0.05 fb, respectively, at $\sqrt{s} = 13\,\text{TeV}$ [3–6], and are concentrated at low values of the VV invariant mass, $m(VV)$. Any significant signal over the prediction, particularly in the high $m(VV)$ tails where the expected SM cross section is small, could indicate BSM physics.

BSM effects on $\gamma\gamma \to VV$ processes are predicted in a variety of models, with both resonant and nonresonant signals [3, 4, 7–13]. A common approach to quantify deviations from the SM with minimal assumptions involves anomalous quartic gauge couplings (AQGCs). Two formalisms commonly used in electroweak studies at the LHC exploit dimension-6 nonlinear operators, and dimension-8 linear operators [14–18], where the terms linear and nonlinear refer to the realization of the broken electroweak symmetry. In the case of the dimension-6 operators, the most general formulation, which was used in the analysis of e^+e^- collisions at LEP [19], has four independent operators. The a_0^W/Λ^2 and a_C^W/Λ^2 operators, where Λ is an energy scale characterizing new physics, will modify the $\gamma\gamma \to WW$ process if they have values different from the SM value of zero. Similarly, nonzero values of the a_0^Z/Λ^2 and a_C^Z/Λ^2 operators will modify the $\gamma\gamma \to ZZ$ process. The detailed definitions of these operators are reported in Refs. [14, 15].

The $\gamma\gamma \to WW$ without the measurement of the outgoing protons was among several processes used to place the first LHC bounds on such AQGCs using 7 and 8 TeV data [20–24]; constraints were also obtained from 1.96 TeV data at the Tevatron [25]. The cross section was also measured at 13 TeV, using the leptonic channel without proton detection [26]. Recently, strong constraints have been placed on AQGCs using a variety of scattering [23, 24, 27–30] and triple boson production [31] processes at 13 TeV. The first limits on anomalous couplings using forward protons measured with PPS were obtained in searches for high-mass $\gamma\gamma \to \gamma\gamma$ scattering [32].

2 Experimental setup

The central feature of the CMS apparatus is a superconducting solenoid of 6 m internal diameter, providing a magnetic field of 3.8 T. Within the solenoid volume are a silicon pixel and strip tracker, a lead tungstate crystal electromagnetic calorimeter (ECAL), and a brass and scintillator hadron calorimeter (HCAL), each composed of a barrel and two endcap sections. Forward calorimeters extend the pseudorapidity (η) coverage provided by the barrel and endcap detectors. Muons are detected in gas-ionization chambers embedded in the steel flux-return yoke outside the solenoid. A more detailed description of the CMS detector, together with a definition of the coordinate system used and the relevant kinematic variables, can be found in Ref. [33].

The Precision Proton Spectrometer is a system of near-beam tracking and timing detectors, located in Roman pots (RPs) at about 200 m from the CMS interaction point [1]. The Roman pots are movable near-beam devices that allow the detectors to be brought very close (within a few mm) to the beam without affecting the vacuum, beam stability, or other aspects of the accelerator operation. The PPS makes it possible to measure the 4-momentum of the scattered protons, along with their time-of-flight from the IP. The proton momenta are measured by two tracking stations on each arm of the spectrometer. The timing, not used for the present

analysis, can be exploited to suppress background from other collisions in the same bunch crossing (pileup).

Events of interest are selected using a two-tiered trigger system. The first level (L1), composed of custom hardware processors, uses information from the calorimeters and muon detectors to select events at a rate of around 100 kHz within a fixed latency of about 4 μs [34]. The second level, known as the high-level trigger (HLT), consists of a farm of processors running a version of the full event reconstruction software optimized for fast processing, and reduces the event rate to around 1 kHz before data storage [35]. The forward proton information from the PPS detector is available in the HLT, but is not used in the HLT selection.

3 Data samples and simulation

The data used for the present analysis were collected at $\sqrt{s} = 13\,\text{TeV}$ in the years 2016–2018. The data are required to pass quality criteria for both PPS and other CMS subdetectors. In the case of PPS, these criteria require the Roman pots to be fully inserted in the data-taking position. Compared with CMS analyses that do not use forward protons, the requirement of having the RPs inserted removes a fraction of data at the beginning and end of each LHC fill. During the first year of operation (2016), a significant amount of time was also devoted to the commissioning of PPS, so the integrated luminosity available for the analysis for that year is only 9.9 fb^{-1}. In the 2017 and 2018 samples, the integrated luminosities of the data meeting the PPS quality criteria are 37.2 fb^{-1} and 52.9 fb^{-1}, respectively, corresponding to nearly 90% of the luminosity available for CMS analyses without forward protons. In total, the three years' data combined correspond to a luminosity of 100 fb^{-1} [36–38].

Signal events are simulated at leading order with the FPMC [5] Monte Carlo (MC) generator, for both the $\gamma\gamma \to \text{WW}$ and $\gamma\gamma \to \text{ZZ}$ channels. The dominant nonexclusive backgrounds from QCD multijet production are simulated at leading order with the PYTHIA 8.205 [39] MC generator with the CUETP8M1 [40] tune for the 2016 samples, and PYTHIA 8.230 with the CP5 [41] tune for the 2017–2018 samples. Backgrounds arising from the production of a W or Z boson in association with jets are simulated at next to leading order (NLO) in QCD with MADGRAPH5_aMC@NLO [42]. The background from pair production of top quarks is simulated at NLO in QCD with POWHEG [43–45]. The parton shower and hadronization for the $\text{W} + \text{jets}$, $\text{Z} + \text{jets}$, and $\text{t}\bar{\text{t}}$ samples are performed with PYTHIA. The SM contribution to the $\gamma\gamma \to \text{WW}$ and $\gamma\gamma \to \text{ZZ}$ processes is expected to be negligible within the kinematic region considered in this analysis.

All of the generated signal and background samples are passed through a detailed GEANT4 [46] simulation of the central part of the CMS detector, extending to $|\eta| < 5$, and reconstructed in the same way as the data. For the signal samples, the forward protons are passed through a "direct" simulation [47], which propagates the protons from the IP to the RP positions, simulates hits in the detector planes, and reconstructs the tracks and proton kinematics in the same way as done for the data. In the background samples, protons from pileup events are not simulated and their effect is estimated from the data, as described later. A realistic mix of beam crossing angles and aperture limitations along the beam line is used when simulating the protons.

4 Event reconstruction

Events are selected online by means of several jet triggers. These are based on either the highest transverse momentum (p_T) jet in the event, or the scalar sum of the p_T values of all jets, H_T.

In some cases, additional requirements on the "trimmed" mass [48] of the jets are imposed, to select jet masses above 30 or 50 GeV. The triggers are identical to those used in the analysis of Ref. [49], where a more detailed description is reported.

The primary vertex (PV) is taken to be the vertex corresponding to the hardest scattering in the event, evaluated using tracking information alone, as described in Section 9.4.1 of Ref. [50].

The particle-flow algorithm [51] reconstructs and identifies each individual particle in an event, with an optimized combination of information from the various elements of the CMS detector. The energy of photons is obtained from the ECAL measurement. The energy of electrons is determined from a combination of the electron momentum at the primary interaction vertex as determined by the tracker, the energy of the corresponding ECAL cluster, and the energy sum of all bremsstrahlung photons spatially compatible with originating from the electron track. The energy of muons is obtained from the curvature of the corresponding track. The energy of charged hadrons is determined from a combination of their momentum measured in the tracker and the matching ECAL and HCAL energy deposits, corrected for the response function of the calorimeters to hadronic showers. Finally, the energy of neutral hadrons is obtained from the corresponding corrected ECAL and HCAL energies.

For each event, hadronic jets are clustered from these reconstructed particles using the infrared and collinear safe anti-k_T algorithm [52], as implemented in the FASTJET package [53], with a distance parameter of 0.8. Jet momentum is determined as the vectorial sum of all particle momenta in the jet, and is found from simulation to be, on average, within 5 to 10% of the true momentum over the whole p_T spectrum and detector acceptance. Additional proton-proton interactions from pileup can contribute with additional tracks and calorimetric energy depositions to the jet momentum. To mitigate this effect, charged particles identified to be originating from pileup vertices are discarded and an offset correction is applied to remove any remaining contributions. Jet energy corrections are derived from simulation to bring the measured response of jets to that of particle-level jets on average. In situ measurements of the momentum balance in dijet, γ + jet, Z + jet, and multijet events are used to account for any residual differences in the jet energy scale between data and simulation [54]. The jet energy resolution amounts typically to 15–20% at 30 GeV, 10% at 100 GeV, and 5% at 1 TeV [54]. Standard CMS quality criteria are applied to each jet to remove jets potentially dominated by spurious contributions from various subdetector components or reconstruction failures.

Hadronic decays of W and Z bosons are identified using the ratio between 2-subjettiness and 1-subjettiness [55], $\tau_{21} = \tau_2/\tau_1$, and the jet mass $m(\mathrm{j})$ after applying a "pruning" algorithm with parameters $D_{\mathrm{cut}} = 0.5m/p_T$, $z_{\mathrm{cut}} = 0.1$ (where m is the mass of the original jet), to reduce the contributions of soft gluon radiation and pileup [56, 57]. The τ_{21} variable is further refined into a τ_{21}^{DDT} variable to reduce the correlation with the jet p_T and mass, by means of the "Designed Decorrelated Taggers" (DDT) approach [49, 58].

Forward protons are reconstructed using a "multi-RP" algorithm, which combines tracks reconstructed in both of the tracking Roman pots in each arm of PPS. The lever arm between the two RPs allows the reconstruction of the proton scattering angles θ^* (where the superscript "*" indicates an angle defined at the IP) and proton fractional momentum loss ξ:

$$\xi = (p_{\mathrm{nom}} - p)/p_{\mathrm{nom}}, \tag{1}$$

where p_{nom} and p are the nominal beam momentum and the scattered proton momentum, respectively. PPS provides a ξ resolution of $\leq$5% over the full acceptance [47]. Additional selections are applied to ensure that the protons are within the acceptance of the sensors, and within the aperture constraints defined by the LHC collimators. The LHC conditions and the

PPS tracking detector configuration were different for each of the three data-taking years. For this reason, the 2016, 2017, and 2018 samples are analyzed separately, and the results are combined at the end. Further details of the proton reconstruction, including the determination of the beam optics and the detector alignment, are presented in [47, 59, 60].

5 Event selection

Events are selected based on the properties of the jets, the protons, and the correlation between protons and jets.

5.1 Jet selection

The jets are first required to have $p_{\mathrm{T}} > 200\,\mathrm{GeV}$, $|\eta| < 2.5$, and, if more than two pass these criteria, the two with the highest p_{T} are chosen. In the following, these are labeled j1 and j2, corresponding to the jet with the highest and second-highest p_{T}, respectively. The pair of jets is required to have a dijet invariant mass $m(\mathrm{jj}) > 1126\,\mathrm{GeV}$, where the efficiency of the trigger is >99% relative to the offline selection [49]. The two jets are further required to have a pseudorapidity difference of $|\Delta\eta| < 1.3$ to reduce the QCD multijets background. Figure 2 shows the dijet invariant mass distribution in data and simulation for each of the three years of data taking in the range of interest.

To enhance the exclusive production, the jets are required to be balanced in azimuthal angle and transverse momentum. This is implemented by requiring the acoplanarity ($a = |1 - (\phi_{\mathrm{j1}} - \phi_{\mathrm{j2}})/\pi|$) is < 0.01, and the ratio ($p_{\mathrm{T}}(\mathrm{j1})/p_{\mathrm{T}}(\mathrm{j2})$) is < 1.3.

Finally, the jet substructure properties are exploited to enrich the sample with merged jets from boosted W or Z decays. The pruned mass of the jets is required to be between 60 and 107 GeV, i.e., compatible with the W or Z mass. The constraint retains almost all signal events. The τ_{21}^{DDT} discriminator must be smaller than 0.75, compatible with that expected for two quark jets originating from one boson decay and merged into a single high-momentum jet. From simulation, this requirement retains approximately 85% of anomalous $\gamma\gamma \to \mathrm{WW}$ events passing all other jet selection criteria, while rejecting ≈65% of high mass QCD multijet background events.

5.2 W and Z selection

The reconstructed pruned mass of the jets discriminates between the WW and ZZ final states, due to the mass difference between the W and Z bosons. To reduce the two-dimensional space of the pruned jet masses (denoted by $m(\mathrm{j1})$ and $m(\mathrm{j2})$) into a single variable, a simple discriminant based on the sum of $m(\mathrm{j1}) + m(\mathrm{j2})$ is used. The result is shown for simulated signal events in Fig. 3, with two distinct distributions visible, corresponding to the WW and ZZ samples. The resolution of the resulting variable is ≈8 GeV for the WW and 10 GeV for the ZZ sample, correspondingly. The optimal value to separate the two channels is then chosen by treating one of the channels as signal and the other as background, and maximizing the signal to background ratio. A value of $m(\mathrm{j1}) + m(\mathrm{j2}) = 166.6\,\mathrm{GeV}$ provides the best separation between WW and ZZ events; this retains more than 80% of signal for each channel, and corresponds to a signal to background ratio of ≈4.8, with no significant dependence on the anomalous coupling values assumed.

5.3 Proton selection

Only protons with a ξ value greater than 0.05 are retained for the analysis to avoid the region of large radiation-induced inefficiencies of the PPS detectors near the beam. For signal events,

the $\xi > 0.05$ requirement is less restrictive than the $m(\mathrm{jj}) > 1126\,\mathrm{GeV}$ condition imposed on the jets. For background events, where the protons are uncorrelated with the jets, the $\xi > 0.05$ and $m(\mathrm{jj}) > 1126\,\mathrm{GeV}$ requirements are independent. The upper bounds imposed by the collimators are different for each of the two arms of the spectrometer, each data-taking period, and each beam crossing angle. The exact upper ξ requirements therefore vary with the data-taking period, generally lying within the range $0.12 \leq \xi \leq 0.20$. The upper mass limit of the centrally produced system (dijet in this analyis) correspondingly varies between 1.55 and 2.01 TeV (for a proton scattering angle of $\theta^* = 0$).

In the 2016 and 2017 data samples, only one proton per event can be reconstructed in each arm of the spectrometer. With improved detectors in 2018, multiple protons can be reconstructed. This leads to an increase in both the expected number of signal events S, and the expected number of background events B. In terms of the expected significance, estimated as $S/\sqrt{B}$, the use of up to three tracks in each arm leads to $\approx$7% improvement over using only events with one track. No additional improvement is seen by using events with more than three tracks, where the effect of showers and noncollision backgrounds becomes significant. Therefore, only events with up to three protons per arm are used, and the proton with the largest value of ξ is chosen for the analysis. The use of multiple-proton events leads to both a significantly larger signal efficiency and a larger combinatorial background in the 2018 data, compared with the 2016 or 2017 data.

5.4 Proton-jet matching and signal region

The matching between the proton and jet kinematics for exclusive signal is based on the variables $1 - m(\mathrm{VV})/m(\mathrm{pp})$ and $y(\mathrm{pp}) - y(\mathrm{VV})$. Here $m(\mathrm{VV})$ and $y(\mathrm{VV})$ represent the invariant mass and rapidity of the WW or ZZ system, as reconstructed from the merged jets. The variables $m(\mathrm{pp})$ and $y(\mathrm{pp})$ are the expected invariant mass and rapidity of the central system, calculated from the proton information:

$$m(\mathrm{pp}) = \sqrt{s}\sqrt{\xi_{\mathrm{p1}}\xi_{\mathrm{p2}}}, \qquad y(\mathrm{pp}) = -\frac{1}{2}\ln\left(\frac{\xi_{\mathrm{p1}}}{\xi_{\mathrm{p2}}}\right). \tag{2}$$

Two signal regions are defined by comparing the invariant mass and rapidity of the WW or ZZ system obtained from the jets with the same quantities inferred from the two protons. A diamond-shaped area in the $y(\mathrm{pp}) - y(\mathrm{VV})$ vs. $1 - m(\mathrm{VV})/m(\mathrm{pp})$ plane, centered around zero, contains the bulk of the signal when both protons are correctly associated to the jets ("region δ"). In case one of the signal protons is missed and a pileup proton is used instead, the events tend to fall in one of the two diagonal bands of Fig. 4. A second signal region ("region o") is therefore defined based on these bands. The dimensions of the two regions are optimized to provide the best expected signal significance, estimated as $S/\sqrt{B}$. Of the simulated signal events passing all other selections, typically between 19% and 25% are contained in region δ, and a similar fraction in region o. The area with $|1 - m(\mathrm{VV})/m(\mathrm{pp})| < 1.0$ and $|y(\mathrm{pp}) - y(\mathrm{VV})| < 0.5$, encompassing both signal regions, remained blinded and was not examined until the selection criteria and background estimation methods were fixed.

6 Background estimation

The background is mainly due to jets produced in one pp collision combined with unrelated protons from pileup interactions in the same bunch crossing. The largest source of jets is QCD multijet production, with smaller contributions from W or Z bosons in association with jets,

and $\mathrm{t\bar{t}}$ production. The protons predominantly arise from diffractive pileup interactions, which are not expected to be well modeled by simulations. For this reason, we rely mainly on data to estimate the background.

The nominal background estimate is derived by inverting the dijet acoplanarity requirements, and/or the dijet-proton matching requirements, to define three independent sideband regions. The first (region B) is defined by acoplanarity $a > 0.01$, with the signal region selection applied in $|1 - m(\mathrm{WW})/m(\mathrm{pp})|$ and $|y(\mathrm{pp}) - y(\mathrm{WW})|$. The second region (region C) has $a < 0.01$, and $|1 - m(\mathrm{WW})/m(\mathrm{pp})| > 1.0$ or $|y(\mathrm{pp}) - y(\mathrm{WW})| > 0.5$. The third (region D) is defined by $a > 0.01$, and $|1 - m(\mathrm{WW})/m(\mathrm{pp})| > 1.0$ or $y(\mathrm{pp}) - y(\mathrm{WW}) > 0.5$. If the numbers of events in each of these regions are N_B, N_C, and N_D, respectively, the expected number of events in the signal region is then $N_\mathrm{A} = (N_\mathrm{B}\, N_\mathrm{C})/N_\mathrm{D}$.

Figure 5 illustrates the distribution of data in these regions for the 2018 data with the WW selection. Data selected with the acoplanarity requirement $a > 0.01$ (referred to as the anti-acoplanarity region/method in the following) are compared with the predicted background from simulation in Fig. 6, for each of the years and in both the WW and ZZ mass regions. In general, the data are well reproduced by the simulation, apart from a small excess at low masses in the 2016 WW sample. Since the final background estimate is obtained entirely from the data, such minor discrepancies do not impact the results.

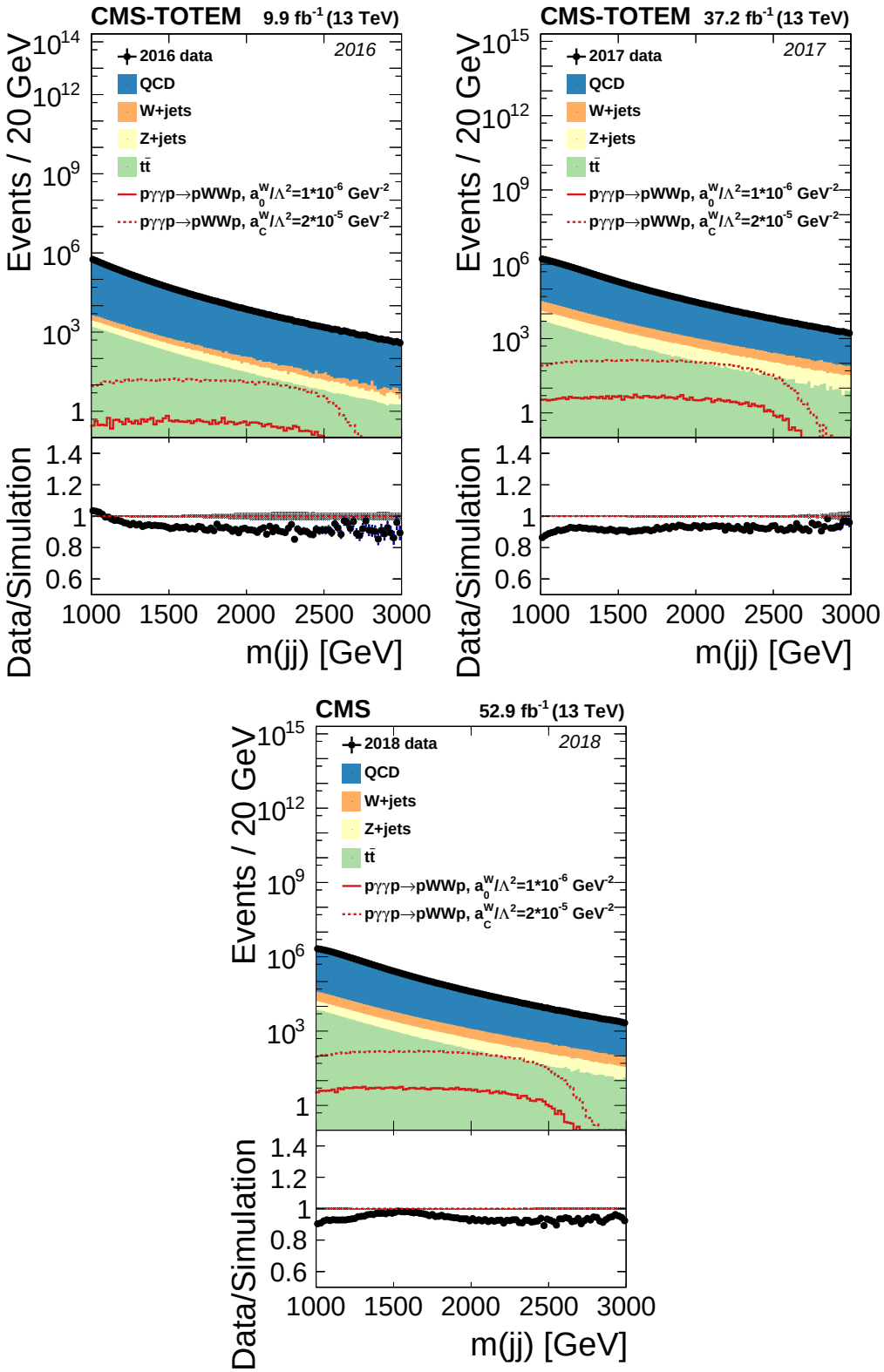

Figure 2: Dijet invariant mass spectra in data and simulation, for the years 2016 (upper left), 2017 (upper right), and 2018 (lower). The distributions of number of events show data compared with the stacked background predictions from simulation, with the corresponding ratios of data to the sum of simulated backgrounds, shown below them. The plots are shown at the preselection level, with no requirements on the protons, jet substructure, or dijet balance. Examples of simulated signals are shown for protons generated in the range of $0.01 \leq \xi \leq 0.20$. Only statistical uncertainties (dashed grey bands) are shown.

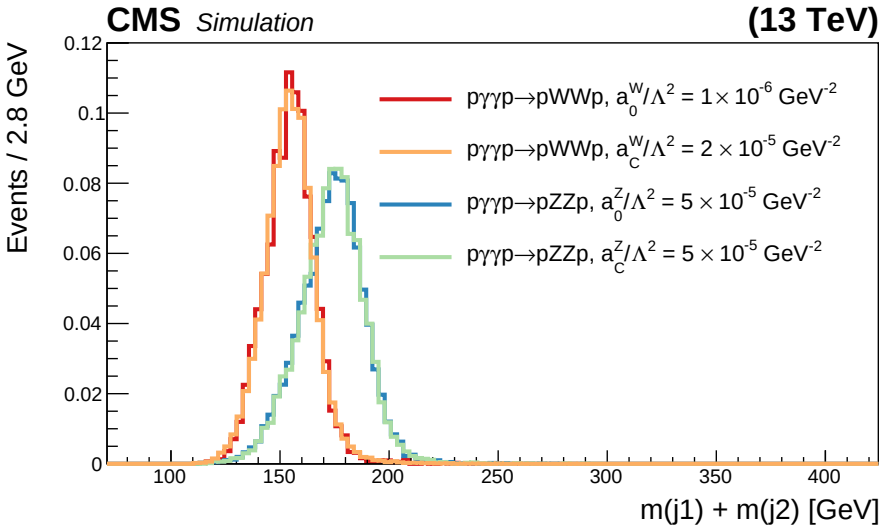

Figure 3: Event distribution as a function of the discriminant described in the text for simulated WW and ZZ signal events.

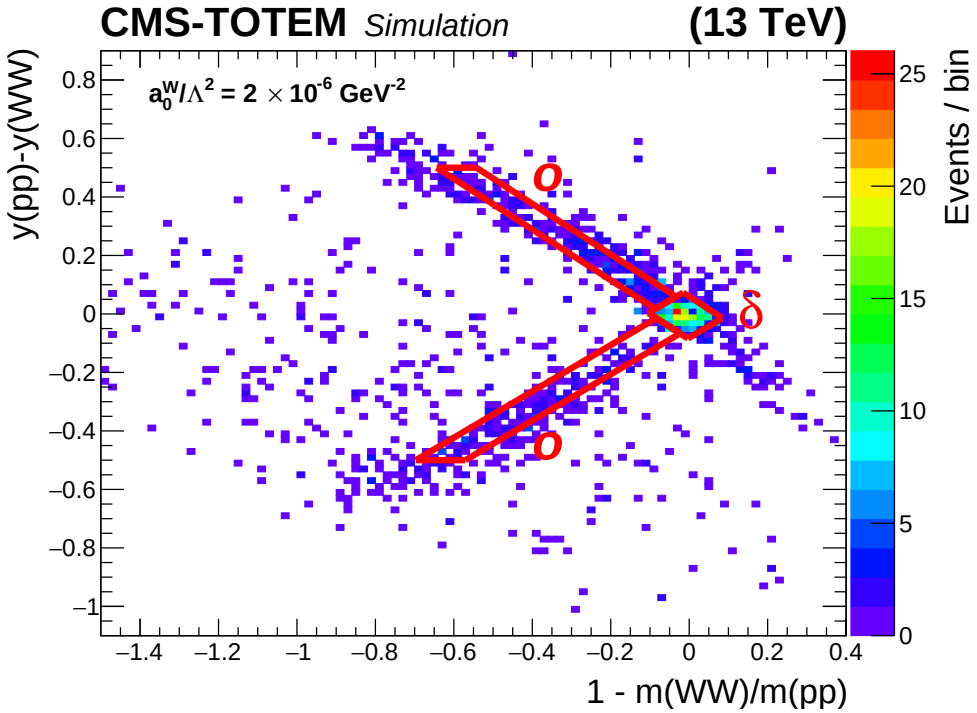

Figure 4: Matching between the jets and the protons, in invariant mass and rapidity, for simulated WW exclusive signal events. The red diamond-shaped area near the origin (signal region δ) corresponds to the case where both protons are correctly matched to the jets. The areas within the red diagonal bands (signal region o) correspond to the case where one proton is correctly matched, and the second proton originates from a pileup interaction.

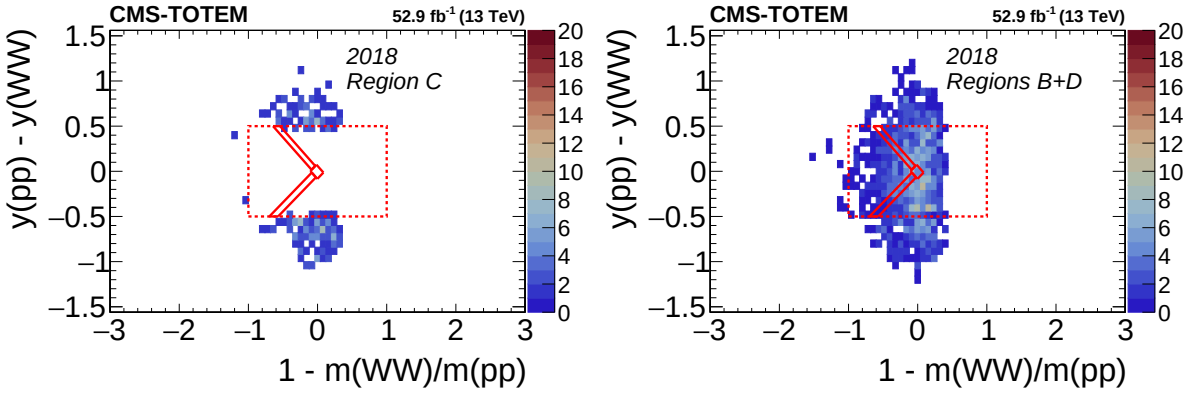

Figure 5: Distribution of the 2018 data in the $y(\mathrm{pp}) - y(\mathrm{VV})$ vs $1 - m(\mathrm{VV})/m(\mathrm{pp})$ plane in the WW mass region. On the left, the sample with all selections applied is shown, except that the region inside the dashed lines remains blinded. On the right, the region with the acoplanarity requirement inverted is shown. The solid lines indicate the same signal regions as shown in Fig. 4. In the right plot the area inside the solid lines corresponds to "region B", while the area outside the dashed lines corresponds to "region D". The color scale on the z axis indicates the number of events in each bin.

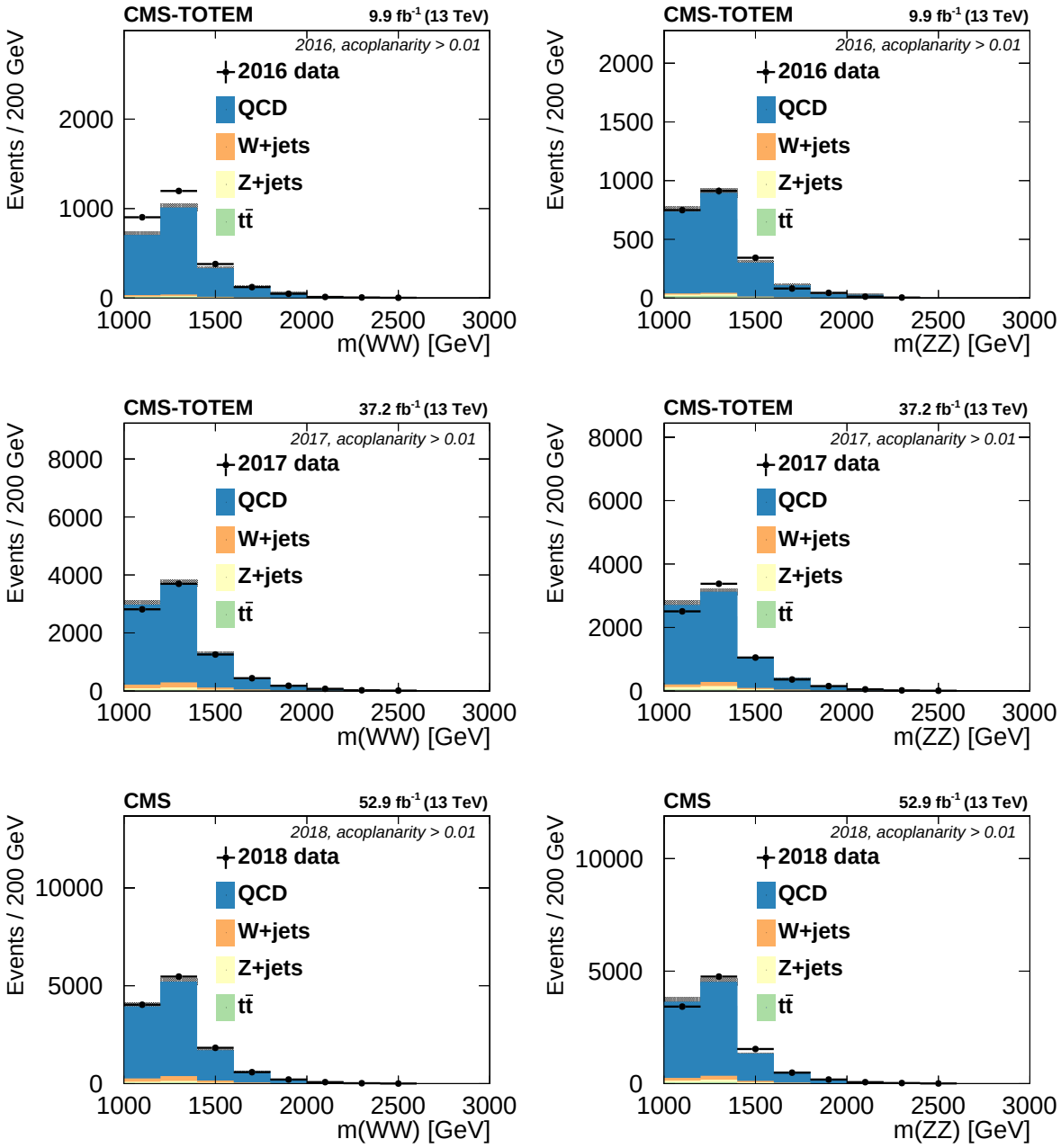

Figure 6: Diboson invariant mass distributions in data and simulation in the anti-acoplanarity region ($a > 0.01$), with no requirement on the proton matching. The plots from top to bottom are for the 2016, 2017, and 2018 data, respectively, with the WW region in the left column and the ZZ region in the right column. Only statistical uncertainties (dashed grey bands) are shown.

As an alternative background model, we perform the same procedure, except that the selection on the pruned masses of both jets is inverted ($m(\mathrm{j}) < 60\,\mathrm{GeV}$ or $m(\mathrm{j}) > 107\,\mathrm{GeV}$), rather than that on the acoplanarity. This method is used only to derive systematic uncertainties.

Finally, as a cross-check we also estimate the background using an event-mixing approach, in which the simulated background events for the central detectors are mixed with protons from real data, randomly drawn from the jet-triggered data sample. This procedure is repeated 1000 times, and the mean and root-mean-square (RMS) of the resulting number of events selected in these pseudoexperiments are taken as the background estimate and uncertainty. In the δ region of the 2016 and 2017 data, the number of expected background events is near zero, and the RMS uncertainties can extend to cover negative values. In these cases we instead consider only the mean and upper limit on the background prediction, where the upper limit is determined by finding the value that contains 95% of the pseudoexperiment results. This procedure has the drawback of relying on simulation for the central jet samples, and explicitly assumes that the protons always originate from different interactions than the jets. Thus, it is not used in the final background estimate, but only as an independent cross-check. Additionally, we use the simulation to perform a closure test of the nominal background estimation method, by using the yields in regions B, C, and D to predict the background in region A, and comparing that prediction with the actual number of simulated background events in region A. No statistically significant differences are observed.

The resulting background estimates and statistical uncertainties, for all years and signal regions, are shown in Tables 1 and 2 for the default method and the alternative method, based on inversions of the acoplanarity and pruned mass requirements, respectively. In these approaches, the origin of the statistical uncertainties is mainly the limited number of events failing the central detector selections but passing the dijet-proton matching ("region B"). The results of the event mixing method are also shown, with statistical uncertainties dominated by the limited number of simulated QCD events. When the event mixing method predicts a small number of background events, only the mean and upper limit are shown.

In general, the estimates obtained from the different methods are compatible, given the statistical uncertainties. In all methods the background is dominated by QCD multijet production, with other backgrounds contributing $\leq$8% of the total, according to the Monte Carlo simulation. The background and expected AQGC signal levels in 2018 are much larger than for the other years. In addition to the increase in integrated luminosity, this reflects the improvements in the PPS tracking detectors and ability to reconstruct multiple protons, which significantly improves the signal efficiency but also increases the number of observed background proton tracks.

7 Systematic uncertainties

We estimate systematic uncertainties in the signal prediction due to the jet energy scale, proton ξ measurement, proton reconstruction efficiency, and integrated luminosity. The effect of the jet energy scale is evaluated by shifting the energy of both jets in the event up or down by the uncertainty, and recomputing the expected signal yields. The resulting uncertainties in the signal yield depend on the data-taking period and sample, but typically range from a few percent up to 10%. Possible discrepancies between data and MC regarding the pruned mass and the τ_{21} variable are found to be negligible (below 1%) using tag and probe method.

The systematic uncertainties related to the proton ξ reconstruction in the two arms are uncorrelated. The effect of this reconstruction uncertainty is evaluated by shifting the value of ξ for

Table 1: Number of background events (N_{evt} with statistical uncertainties) expected for all methods in the different WW analysis regions with reconstruction of both signal protons (region δ) or only one signal proton (region o). The mean value of the expected number of signal events for one anomalous coupling point ($a_0^{\text{W}}/\Lambda^2 = 5 \times 10^{-6}\,\text{GeV}^{-2}$) and for the SM are also shown for comparison. In cases where zero simulated SM events pass the final selection, the value is displayed as a 95% confidence level upper limit.

Number of events	region	N_{evt} (2016)	N_{evt} (2017)	N_{evt} (2018)
Anti-acoplanarity sideband	δ	0.4 ± 0.4	1.6 ± 1.0	11.6 ± 2.6
Anti-pruned mass sideband	δ	0.5 ± 0.2	1.5 ± 0.3	11.3 ± 0.8
Event mixing	δ	0.5 (< 2.2)	1.8 (< 4.2)	14.3 ± 8.9
Expected signal ($a_0^{\text{W}}/\Lambda^2 = 5 \times 10^{-6}\,\text{GeV}^{-2}$)	δ	1.7	2.2	16.1
Expected signal (SM)	δ	0.006	< 0.05	0.03
Anti-acoplanarity sideband	o	1.4 ± 0.9	10.0 ± 3.2	41.4 ± 5.7
Anti-pruned mass sideband	o	2.5 ± 0.8	7.1 ± 1.3	43.0 ± 3.0
Event mixing	o	2.4 ± 1.9	8.4 ± 6.3	49 ± 13
Expected signal ($a_0^{\text{W}}/\Lambda^2 = 5 \times 10^{-6}\,\text{GeV}^{-2}$)	o	1.5	1.7	16.8
Expected signal (SM)	o	0.005	< 0.05	< 0.07

each simulated signal proton by an amount drawn from a Gaussian distribution with width equal to the uncertainty [47], and recomputing the expected signal yield. Because of the tight matching requirements between protons and jets, this is one of the largest systematic uncertainties in the analysis, with values typically of the order of 30% of the expected signal yield. The proton reconstruction efficiency uncertainties are based on comparing results obtained with different control samples and efficiency estimation procedures [47]. The total efficiency uncertainty per arm is 10% in 2016; in 2017 and 2018 the improved detectors and methods led to uncertainties between 2 and 3% per arm [47]. The efficiency uncertainties for the two arms are assumed uncorrelated, and are summed in quadrature to obtain the event uncertainty. The integrated luminosity uncertainties are estimated as 1.2% [36], 2.3% [37], and 2.5% [38] for the 2016, 2017, and 2018 samples, respectively. The uncertainty includes both a part that is uncorrelated between years, and parts that are correlated between 2016 and 2017, and between 2016, 2017, and 2018. The overall uncertainty for the 2016–2018 period for data collected with PPS is 1.8%.

The theoretical uncertainty in the signal prediction includes contributions from the simulation sample size, and from the proton survival probability, i.e., the probability that the colliding protons do not break up due to soft interactions between their spectator partons. The statistical uncertainty in the simulation varies with the assumed anomalous coupling value and year simulated. For the points closest to the expected sensitivity, which determine the numerical value of the limits, it is typically in the range of 2–10%. For the smallest coupling values simulated, which are far from the expected sensitivity, it is typically 25% in the 2016 samples where the integrated luminosity of the data is low. The uncertainty in the proton survival probability is assumed to be 10% [61].

The systematic uncertainty in the background has two contributions. The first is the statistical uncertainty in the normalization, based on the nominal acoplanarity sideband method. The

Table 2: Number of background events (N_{evt} with statistical uncertainties) expected for all methods in the different ZZ analysis regions with reconstruction of both signal protons (region δ) or only one signal proton (region o). The mean value of the expected number of the expected signal for one anomalous coupling point ($a_0^Z/\Lambda^2 = 1 \times 10^{-5}\,\text{GeV}^{-2}$) is also shown for comparison.

Number of events	region	N_{evt} (2016)	N_{evt} (2017)	N_{evt} (2018)
Anti-acoplanarity sideband	δ	1.5 ± 1.1	1.6 ± 0.8	14.2 ± 3.0
Anti-pruned mass sideband	δ	0.4 ± 0.2	0.9 ± 0.2	9.9 ± 0.9
Event mixing	δ	0.5 (< 2.1)	1.5 (< 3.6)	11.6 ± 9.4
Expected signal ($a_0^Z/\Lambda^2 = 1 \times 10^{-5}\,\text{GeV}^{-2}$)	δ	1.3	1.4	9.0
Anti-acoplanarity sideband	o	1.5 ± 1.1	3.7 ± 1.5	37.4 ± 5.6
Anti-pruned mass sideband	o	2.1 ± 0.8	5.4 ± 1.3	41.7 ± 3.1
Event mixing	o	2.0 ± 1.8	6.3 ± 5.1	42 ± 16
Expected signal ($a_0^Z/\Lambda^2 = 1 \times 10^{-5}\,\text{GeV}^{-2}$)	o	1.0	1.6	12.8

second is the dependence of the background estimate on the choice of the sideband region. This is estimated as the full difference between the central values of the acoplanarity sideband method, and the pruned mass sideband method. The first uncertainty, which depends mainly on the amount of sideband data, ranges from $\approx 15 - 20\%$ in the 2018 data, to $>100\%$ in the 2016 data. The second uncertainty also has a significant statistical component, which ranges from a few percent in the 2018 data, to 80% in the 2016 data.

8 Signal extraction and results

The high-mass exclusive $\gamma\gamma \to$ WW and $\gamma\gamma \to$ ZZ signals are extracted using a binned maximum-likelihood fit in a total of twelve bins: one for each of the three years of data taking, times two for the WW and ZZ regions, times two for the events with either reconstruction of both signal protons (region δ) or only one signal proton (region o). In most cases, systematic uncertainties are included as log-normal nuisance parameters [62]. When the estimate of the systematic uncertainty is based on a sample with less than 10 events, Poisson nuisances are used instead; this applies to some of the background statistical uncertainties derived from sideband regions, and some of the simulation statistical errors for very small couplings. The signal is estimated for each of the anomalous couplings, with all other couplings fixed to zero.

Figure 7 shows the number of observed events compared with the expected background and a hypothetical signal, in each bin of the analysis. The backgrounds and observed data are compared with a signal having nonzero WW anomalous couplings, slightly above the expected sensitivity of the analysis. Small ($\leq 1\sigma$) excesses are seen in "region o" of the WW for all years, while small deficits are seen in the ZZ channel. None of these excesses or deficits in the data are significant.

8.1 AQGC limits

The resulting expected and observed 95% confidence level (CL) upper limits on the AQGC operators are shown in Fig. 8.

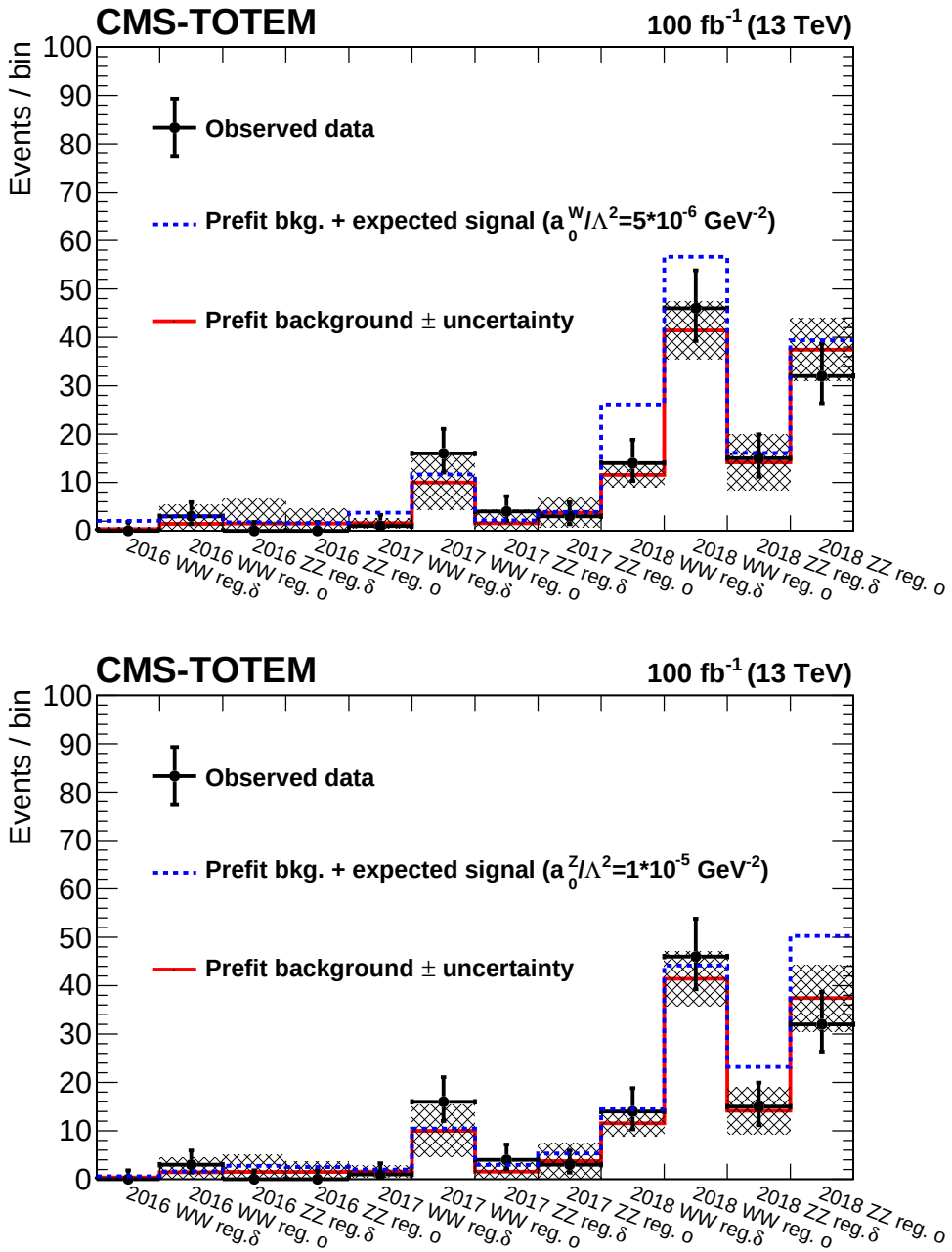

Figure 7: Observed data and expected number of background events in each signal region. Hypothetical AQGC signals are also shown. The histogram with solid lines indicates the number expected for only background, with uncertainties shown by the shaded band. The dashed-line histogram shows the number for background plus assumed signals with $a_0^{\mathrm{W}}/\Lambda^2 = 5 \times 10^{-6}\,\mathrm{GeV}^{-2}$ (upper) or $a_0^{\mathrm{Z}}/\Lambda^2 = 1 \times 10^{-5}\,\mathrm{GeV}^{-2}$ (lower). The histograms and uncertainties are shown prior to the binned maximum-likelihood fit described in the text. The shaded band indicates the uncertainty in the background estimate, while the vertical bars on the points represent the statistical uncertainty in the observed data.

For large values of anomalous couplings, the predicted cross section becomes unphysically large at high masses of the produced diboson system, and violates partial wave unitarity. We estimate the sensitivity of the limits to this effect by calculating the energy of $\gamma\gamma$ collisions

Table 3: Limits on LEP-like dimension-6 anomalous quartic gauge coupling parameters [19], with and without unitarization via a clipping [27] procedure.

Coupling	Observed (expected) 95% CL upper limit No clipping	Observed (expected) 95% CL upper limit Clipping at 1.4 TeV
$\lvert a_0^W/\Lambda^2\rvert$	4.3 (3.9) $\times 10^{-6}\,\text{GeV}^{-2}$	5.2 (5.1) $\times 10^{-6}\,\text{GeV}^{-2}$
$\lvert a_C^W/\Lambda^2\rvert$	1.6 (1.4) $\times 10^{-5}\,\text{GeV}^{-2}$	2.0 (2.0) $\times 10^{-5}\,\text{GeV}^{-2}$
$\lvert a_0^Z/\Lambda^2\rvert$	0.9 (1.0) $\times 10^{-5}\,\text{GeV}^{-2}$	—
$\lvert a_C^Z/\Lambda^2\rvert$	4.0 (4.5) $\times 10^{-5}\,\text{GeV}^{-2}$	—

at which unitarity is violated for the expected limits [17], and then apply a "clipping" procedure [27] to remove the simulated signal above that value. The background estimate and the data are left unchanged in this procedure. In Ref. [27] the SM contribution to the signal was retained above the clipping threshold; in the current analysis the total SM signal is negligible, and is not included. We then rederive the limits with the clipping applied.

In the WW channel, unitarity violation occurs at a diboson mass of $\Lambda \approx 1.4\,\text{TeV}$. By clipping the signal model at that value, we obtain new expected limits that are approximately 30 to 40% higher than the unitarity-violating limits. In the ZZ channel, where the expected limits are higher, unitarity violation occurs at approximately 1.1 TeV for both a_0^Z/Λ^2 and a_C^Z/Λ^2. In this case, because of the invariant mass threshold imposed by the jet triggers, there is no value of clipping for which unitarity is preserved. The full list of 95% CL upper limits with and without clipping is shown in Table 3.

We also obtain limits in the two-dimensional planes of a_0^W/Λ^2 vs. a_C^W/Λ^2 and a_0^Z/Λ^2 vs. a_C^Z/Λ^2 by fitting the limits on the ratio of observed to predicted cross sections to an analytical model for the dependence of the cross section on the AQGC values. The results are shown in Fig. 9. The a_0^W/Λ^2 vs. a_C^W/Λ^2 limits are shown with and without clipping the signal model at 1.4 TeV. Compared with the limits on the $|a_0^W/\Lambda^2|$ and $|a_C^W/\Lambda^2|$ couplings obtained with LHC Run 1 data [20, 22], where unitarization was imposed via a dipole form factor, the unitarized limits obtained here represent an improvement by a factor ≈15–20.

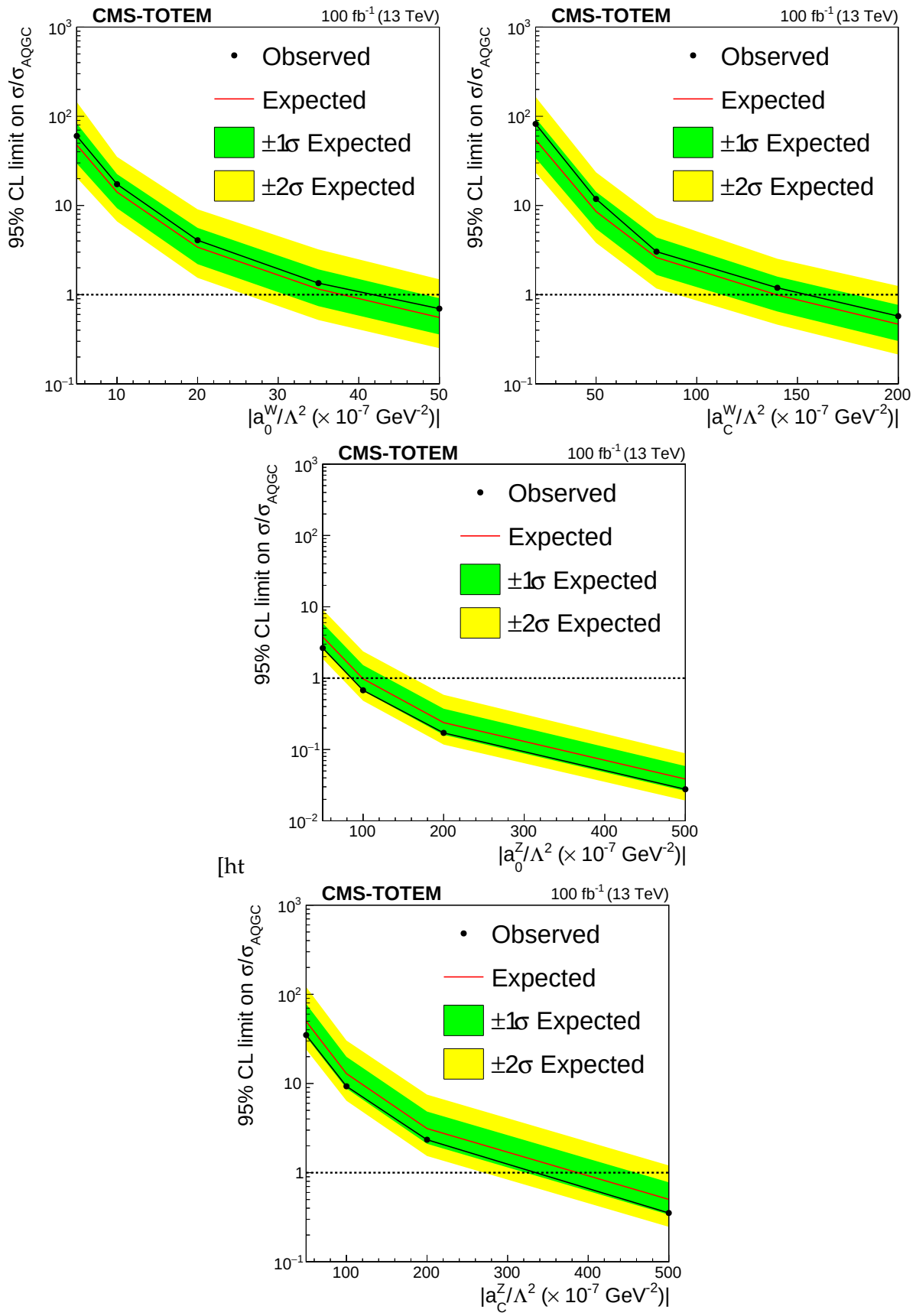

[ht

Figure 8: Expected and observed upper limits on the AQGC operators a_0^W/Λ^2 (upper left), a_C^W/Λ^2 (upper right), a_0^Z/Λ^2 (lower left), a_C^Z/Λ^2 (lower right), with no unitarization. The y axis shows the limit on the ratio of the observed cross section to the cross section predicted for each anomalous coupling value (σ_{AQGC}).

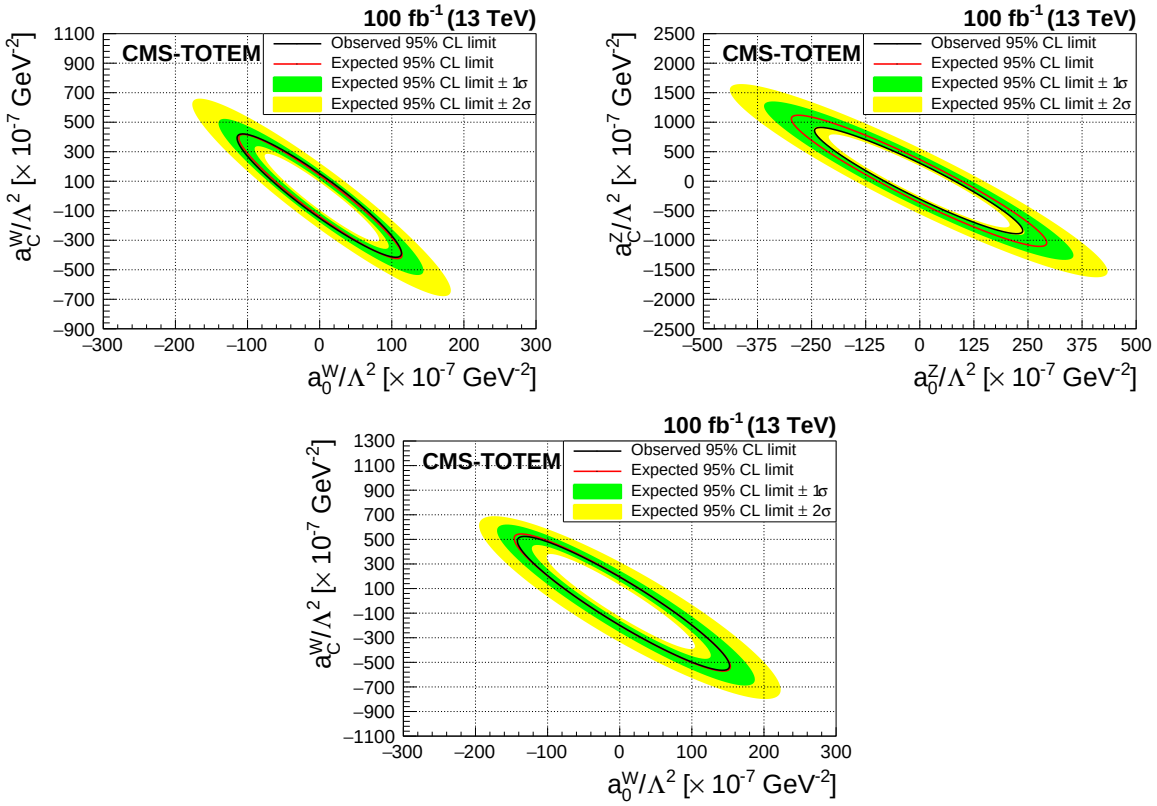

Figure 9: Expected and observed limits in the two-dimensional plane of a_0^W/Λ^2 vs a_C^W/Λ^2 (upper left), a_0^Z/Λ^2 vs. a_C^Z/Λ^2 (upper right), and a_0^W/Λ^2 vs. a_C^W/Λ^2 with unitarization imposed by clipping the signal model at 1.4 TeV (lower).

8.2 Translation to linear dimension-8 AQGCs

Many recent anomalous coupling searches quote limits on dimension-8 linear operators alone. These operators are classified in several categories, depending on whether they contain only covariant derivatives of the Higgs field, only field strength tensors, or both ("mixed" operators, with couplings denoted f_M) [18]. In the case of processes involving photons, the $a_{0,C}^{\mathrm{W,Z}}$ operators can be translated into a linear combination of "mixed" dimension-8 $f_{M,i}\,(i = 0\text{–}7)$ operators [18]. For the a_0^{W} coupling, the relationship reads [18]:

$$a_0^{\mathrm{W}} = -\frac{m_{\mathrm{W}}}{\pi\alpha_{\mathrm{em}}}\left[s_w^2\frac{f_{M,0}}{\Lambda^2} + 2c_w^2\frac{f_{M,2}}{\Lambda^2} + s_w c_w\frac{f_{M,4}}{\Lambda^2}\right]. \tag{3}$$

Here m_{W} is the W boson mass, α_{em} is the fine structure constant, and s_w and c_w represent the sine and cosine of the weak mixing angle, respectively. By further assuming that anomalous contributions to WWZγ vanish, an additional constraint of $f_{M,0} + 2f_{M,2}$ is obtained [14, 63], allowing a_0^{W} to be written in terms of only $f_{M,0}$ and $f_{M,4}$. In order to compare with other results, we scan the values of $f_{M,0}$ and $f_{M,4}$ for which the limit on a_0^{W} is satisfied. We find the results shown in Table 4, evaluated at the point where the other coupling is zero.

Table 4: Conversion of limits on a_0^{W} to dimension-8 $f_{M,i}$ operators, using the assumption of vanishing WWZγ couplings to eliminate some parameters. When quoting limits on one of the operators, the other is fixed to zero. The results for $|f_{M,0}/\Lambda^4|$ and $|f_{M,4}/\Lambda^4|$ are shown with and without clipping of the signal model at 1.4 TeV, when the other parameter is fixed to the SM value of zero.

Coupling	Observed (expected) 95% CL upper limit No clipping	Observed (expected) 95% CL upper limit Clipping at 1.4 TeV
$\lvert f_{M,0}/\Lambda^4\rvert$	16.2 (14.7) TeV^{-4}	19.5 (19.2) TeV^{-4}
$\lvert f_{M,4}/\Lambda^4\rvert$	90.9 (82.6) TeV^{-4}	110 (108) TeV^{-4}

Alternatively, all dimension-8 $f_{M,i}$ except one are set equal to zero. In this case, the results of the conversion are shown in Table 5.

The results are compared with other vector boson scattering studies at 13 TeV that are sensitive to the same operators [28]. When the conversion is performed assuming vanishing WWZγ couplings, the unitarity-violating limits on $|f_{M,0}/\Lambda^4|$ and $|f_{M,4}/\Lambda^4|$ are several times looser than those quoted in other measurements. After the clipping, the results for $|f_{M,0}/\Lambda^4|$ are similar to the best limits obtained from vector boson scattering in the same sign $\mathrm{W}^{\pm}\mathrm{W}^{\pm}$ and WZ final states in CMS [27]. The milder effect of the unitarization in this analysis is due to the upper mass limit of $\approx$2 TeV for reconstructing the protons, imposed by the LHC collimator apertures. This already suppresses most of the unphysical high-mass part of the signal model, before applying any unitarization procedure.

When the conversion is performed by setting all other couplings to zero, the limits on $|f_{M,0}/\Lambda^4|$ are significantly looser, the limits on $|f_{M,4}/\Lambda^4|$ are somewhat more restrictive, and tight constraints are obtained on $|f_{M,2}/\Lambda^4|$.

Table 5: Conversion of limits on a_0^W and a_C^W to dimension-8 $f_{M,i}$ operators, using the assumption that all $f_{M,i}$ except one are equal to zero. The results are shown with and without clipping of the signal model at 1.4 TeV.

Coupling	Observed (expected) 95% CL upper limit No clipping	Observed (expected) 95% CL upper limit Clipping at 1.4 TeV
$\lvert f_{M,0}/\Lambda^4\rvert$	66.0 (60.0) TeV^{-4}	79.8 (78.2) TeV^{-4}
$\lvert f_{M,1}/\Lambda^4\rvert$	245.5 (214.8) TeV^{-4}	306.8 (306.8) TeV^{-4}
$\lvert f_{M,2}/\Lambda^4\rvert$	9.8 (9.0) TeV^{-4}	11.9 (11.8) TeV^{-4}
$\lvert f_{M,3}/\Lambda^4\rvert$	73.0 (64.6) TeV^{-4}	91.3 (92.3) TeV^{-4}
$\lvert f_{M,4}/\Lambda^4\rvert$	36.0 (32.9) TeV^{-4}	43.5 (42.9) TeV^{-4}
$\lvert f_{M,5}/\Lambda^4\rvert$	67.0 (58.9) TeV^{-4}	83.7 (84.1) TeV^{-4}
$\lvert f_{M,7}/\Lambda^4\rvert$	490.9 (429.6) TeV^{-4}	613.7 (613.7) TeV^{-4}

8.3 Fiducial cross sections

In addition to the limits on different anomalous coupling parameters, we derive upper limits on the cross section for an AQGC-like signal in the $\text{pp} \to \text{pWWp}$ and $\text{pp} \to \text{pZZp}$ channels. The limits are obtained for a fiducial region of $0.04 < \xi < 0.20$ and diboson invariant mass $m(\text{VV}) > 1\,\text{TeV}$, and correspond to the diboson production cross section before decays into hadrons. The signal simulation is used to extrapolate from the measurement region to the fiducial region. As with the AQGC limits, the cross section limits are obtained for each channel separately, assuming zero signal in the other channel. After verifying that the signal efficiency and acceptance do not depend strongly on the exact value of the AQGCs, for $0.04 < \xi < 0.20$ and $m(\text{VV}) > 1000\,\text{GeV}$ we measure the following upper exclusion limits at 95% CL: $\sigma(\text{pp} \to \text{pWWp}) < 67(53^{+34}_{-19})$ fb and $\sigma(\text{pp} \to \text{pZZp}) < 43(62^{+33}_{-20})$ fb, where the expected limit and its one standard deviation uncertainty are shown in parentheses.

9 Summary

A first search for exclusive high-mass $\gamma\gamma \to \text{WW}$ and $\gamma\gamma \to \text{ZZ}$ production with reconstructed forward protons has been performed, in final states with hadronically decaying W or Z bosons, using $100\,\text{fb}^{-1}$ of data collected in 13 TeV proton-proton collisions. No significant excess is found over the standard model background prediction. The resulting limits are interpreted in terms of nonlinear dimension-6 and linear dimension-8 anomalous quartic gauge couplings (AQGC).

The unitarized dimension-6 $\gamma\gamma\text{WW}$ AQGC limits are approximately 15–20 times more stringent than those obtained from the $\gamma\gamma \to \text{WW}$ process without proton detection using the LHC Run 1 data [20, 22]. The derived dimension-8 limits are close to those obtained from same-sign WW and WZ scattering at 13 TeV after unitarization, for the case when the $\text{WWZ}\gamma$ coupling is suppressed. The limits on $\gamma\gamma\text{ZZ}$ anomalous couplings are the first obtained from the exclusive $\gamma\gamma \to \text{ZZ}$ channel. New limits are placed on the cross section in a fiducial region of $0.04 < \xi < 0.20$ and diboson invariant mass $m(\text{VV}) > 1\,\text{TeV}$ of $\gamma\gamma \to \text{WW}$ and $\gamma\gamma \to \text{ZZ}$ production with intact forward protons.

Tabulated results are provided in HEPData [64].

References

[1] CMS and TOTEM Collaborations, "CMS-TOTEM Precision Proton Spectrometer", Technical Report CERN-LHCC-2014-021, TOTEM-TDR-003, CMS-TDR-13, 2014.

[2] CMS and TOTEM Collaboration, "Observation of proton-tagged, central (semi)exclusive production of high-mass lepton pairs in pp collisions at 13 TeV with the CMS-TOTEM precision proton spectrometer", *JHEP* **07** (2018) 153, doi:10.1007/JHEP07(2018)153, arXiv:1803.04496.

[3] E. Chapon, C. Royon, and O. Kepka, "Anomalous quartic WW$\gamma\gamma$, ZZ$\gamma\gamma$, and trilinear WWγ couplings in two-photon processes at high luminosity at the LHC", *Phys. Rev. D* **81** (2010) 074003, doi:10.1103/physrevd.81.074003, arXiv:0912.5161.

[4] C. Baldenegro, G. Biagi, G. Legras, and C. Royon, "Central exclusive production of W boson pairs in pp collisions at the LHC in hadronic and semi-leptonic final states", *JHEP* **12** (2020) 165, doi:10.1007/JHEP12(2020)165, arXiv:2009.08331.

[5] M. Boonekamp et al., "FPMC: a generator for forward physics", 2011. arXiv:1102.2531.

[6] H.-S. Shao and D. d'Enterria, "gamma-UPC: automated generation of exclusive photon-photon processes in ultraperipheral proton and nuclear collisions with varying form factors", *JHEP* **09** (2022) 248, doi:10.1007/JHEP09(2022)248, arXiv:2207.03012.

[7] T. Pierzchala and K. Piotrzkowski, "Sensitivity to anomalous quartic gauge couplings in photon-photon interactions at the LHC", *Nucl. Phys. Proc. Suppl.* **179-180** (2008) 257, doi:10.1016/j.nuclphysbps.2008.07.032, arXiv:0807.1121.

[8] M. Maniatis, A. von Manteuffel, and O. Nachtmann, "Anomalous couplings in $\gamma\gamma \to W^+W^-$ at LHC and ILC", *Nucl. Phys. Proc. Suppl.* **179-180** (2008) 104, doi:10.1016/j.nuclphysbps.2008.07.012.

[9] R. L. Delgado, A. Dobado, M. J. Herrero, and J. J. Sanz-Cillero, "One-loop $\gamma\gamma \to {W^+}_L{W^-}_L$ and $\gamma\gamma \to Z_L Z_L$ from the electroweak chiral lagrangian with a light Higgs-like scalar", *JHEP* **07** (2014) 149, doi:10.1007/JHEP07(2014)149, arXiv:1404.2866.

[10] S. Fichet and G. von Gersdorff, "Anomalous gauge couplings from composite Higgs and warped extra dimensions", *JHEP* **03** (2014) 102, doi:10.1007/JHEP03(2014)102, arXiv:1311.6815.

[11] R. S. Gupta, "Probing quartic neutral gauge boson couplings using diffractive photon fusion at the LHC", *Phys. Rev. D* **85** (2012) 014006, doi:10.1103/PhysRevD.85.014006, arXiv:1111.3354.

[12] R. L. Delgado et al., "Collider production of electroweak resonances from $\gamma\gamma$ states", *JHEP* **11** (2018) 010, doi:10.1007/JHEP11(2018)010, arXiv:1710.07548.

[13] R. L. Delgado, A. Dobado, and F. J. Llanes-Estrada, "Coupling WW, ZZ unitarized amplitudes to $\gamma\gamma$ in the TeV region", *Eur. Phys. J. C* **77** (2017) 205, doi:10.1140/epjc/s10052-017-4768-y, arXiv:1609.06206.

[14] G. Bélanger et al., "Bosonic quartic couplings at LEP2", *Eur. Phys. J. C* **13** (2000) 283, doi:10.1007/s100520000305, arXiv:hep-ph/9908254.

[15] G. Bélanger and F. Boudjema, "$\gamma\gamma \to W^+W^-$ and $\gamma\gamma \to ZZ$ as tests of novel quartic couplings", *Phys. Lett. B* **288** (1992) 210, doi:10.1016/0370-2693(92)91979-J.

[16] O. J. P. Éboli, M. C. Gonzalez-Garcia, and J. K. Mizukoshi, "$pp \to jje^{\pm}\mu^{\pm}\nu\nu$ and $jje^{\pm}\mu^{\mp}\nu\nu$ at $\mathcal{O}(\alpha_{em}^6)$ and $\mathcal{O}(\alpha_{em}^4\alpha_s^2)$ for the study of the quartic electroweak gauge boson vertex at CERN LHC", *Phys. Rev. D* **74** (2006) 073005, doi:10.1103/PhysRevD.74.073005.

[17] O. J. P. Éboli, M. C. Gonzalez-Garcia, and S. M. Lietti, "Bosonic quartic couplings at CERN LHC", *Phys. Rev. D* **69** (2004) 095005, doi:10.1103/PhysRevD.69.095005, arXiv:hep-ph/0310141.

[18] O. J. P. Éboli and M. C. Gonzalez-Garcia, "Classifying the bosonic quartic couplings", *Phys. Rev. D* **93** (2016) 093013, doi:10.1103/PhysRevD.93.093013, arXiv:1604.03555.

[19] OPAL Collaboration, "Constraints on anomalous quartic gauge boson couplings from $\nu\bar{\nu}\gamma\gamma$ and $q\bar{q}\gamma\gamma$ events at CERN LEP2", *Phys. Rev. D* **70** (2004) 032005, doi:10.1103/PhysRevD.70.032005, arXiv:hep-ex/0402021.

[20] ATLAS Collaboration, "Measurement of exclusive $\gamma\gamma \to W^+W^-$ production and search for exclusive Higgs boson production in pp collisions at $\sqrt{s} = 8$ TeV using the ATLAS detector", *Phys. Rev. D* **94** (2016) 032011, doi:10.1103/PhysRevD.94.032011, arXiv:1607.03745.

[21] CMS Collaboration, "Study of exclusive two-photon production of W^+W^- in pp collisions at $\sqrt{s} = 7$ TeV and constraints on anomalous quartic gauge couplings", *JHEP* **07** (2013) 116, doi:10.1007/JHEP07(2013)116, arXiv:1305.5596.

[22] CMS Collaboration, "Evidence for exclusive $\gamma\gamma \to W^+W^-$ production and constraints on anomalous quartic gauge couplings in pp collisions at $\sqrt{s} = 7$ and 8 TeV", *JHEP* **08** (2016) 119, doi:10.1007/JHEP08(2016)119, arXiv:1604.04464.

[23] CMS Collaboration, "Observation of electroweak production of same-sign W boson pairs in the two jet and two same-sign lepton final state in proton-proton collisions at $\sqrt{s} = 13$ TeV", *Phys. Rev. Lett.* **120** (2018) 081801, doi:10.1103/PhysRevLett.120.081801, arXiv:1709.05822.

[24] CMS Collaboration, "Evidence for electroweak production of four charged leptons and two jets in proton-proton collisions at $\sqrt{s} = 13$ TeV", *Phys. Lett. B* **812** (2020) 135992, doi:j.physletb.2020.135992, arXiv:2008.07013.

[25] D0 Collaboration, "Search for anomalous quartic $WW\gamma\gamma$ couplings in dielectron and missing energy final states in $p\bar{p}$ collisions at $\sqrt{s} = 1.96$ TeV", *Phys. Rev. D* **88** (2013) 012005, doi:10.1103/PhysRevD.88.012005, arXiv:1305.1258.

[26] ATLAS Collaboration, "Observation of photon-induced W^+W^- production in pp collisions at $\sqrt{s} = 13$ TeV using the ATLAS detector", *Phys. Lett. B* **816** (2021) 136190, doi:10.1016/j.physletb.2021.136190, arXiv:2010.04019.

[27] CMS Collaboration, "Measurements of production cross sections of WZ and same-sign WW boson pairs in association with two jets in proton-proton collisions at $\sqrt{s} = 13\,\text{TeV}$", *Phys. Lett. B* **809** (2020) 135710, doi:10.1016/j.physletb.2020.135710, arXiv:2005.01173.

[28] CMS Collaboration, "Measurement of the electroweak production of $Z\gamma$ and two jets in proton-proton collisions at $\sqrt{s} = 13\,\text{TeV}$ and constraints on anomalous quartic gauge couplings", *Phys. Rev. D* **104** (2021) 072001, doi:10.1103/PhysRevD.104.072001, arXiv:2106.11082.

[29] CMS Collaboration, "Observation of electroweak production of $W\gamma$ with two jets in proton-proton collisions at $\sqrt{s} = 13\,\text{TeV}$", *Phys. Lett. B* **811** (2020) 135988, doi:10.1016/j.physletb.2020.135988, arXiv:2008.10521.

[30] CMS Collaboration, "Measurement of vector boson scattering and constraints on anomalous quartic couplings from events with four leptons and two jets in proton-proton collisions at $\sqrt{s} = 13\,\text{TeV}$", *Phys. Lett. B* **774** (2017) 682, doi:10.1016/j.physletb.2017.10.020, arXiv:1708.02812.

[31] CMS Collaboration, "Measurements of the $\text{pp} \to \text{W}^{\pm}\gamma\gamma$ and $\text{pp} \to \text{Z}\gamma\gamma$ cross sections at $\sqrt{s} = 13\,\text{TeV}$ and limits on anomalous quartic gauge couplings", *JHEP* **10** (2021) 174, doi:10.1007/JHEP10(2021)174, arXiv:2105.12780.

[32] CMS and TOTEM Collaboration, "First search for exclusive diphoton production at high mass with tagged protons in proton-proton collisions at $\sqrt{s} = 13\,\text{TeV}$", *Phys. Rev. Lett.* **129** (2022) 011801, doi:10.1103/PhysRevLett.129.011801, arXiv:2110.05916.

[33] CMS Collaboration, "The CMS experiment at the CERN LHC", *JINST* **3** (2008) S08004, doi:10.1088/1748-0221/3/08/S08004.

[34] CMS Collaboration, "Performance of the CMS Level-1 trigger in proton-proton collisions at $\sqrt{s} = 13\,\text{TeV}$", *JINST* **15** (2020) P10017, doi:10.1088/1748-0221/15/10/P10017, arXiv:2006.10165.

[35] CMS Collaboration, "The CMS trigger system", *JINST* **12** (2017) P01020, doi:10.1088/1748-0221/12/01/P01020, arXiv:1609.02366.

[36] CMS Collaboration, "Precision luminosity measurement in proton-proton collisions at $\sqrt{s} = 13\,\text{TeV}$ in 2015 and 2016 at CMS", *Eur. Phys. J. C* **81** (2021) 800, doi:10.1140/epjc/s10052-021-09538-2, arXiv:2104.01927.

[37] CMS Collaboration, "CMS luminosity measurement for the 2017 data-taking period at $\sqrt{s} = 13\,\text{TeV}$", CMS Physics Analysis Summary CMS-PAS-LUM-17-004, CERN, Geneva, 2018.

[38] CMS Collaboration, "CMS luminosity measurement for the 2018 data-taking period at $\sqrt{s} = 13\,\text{TeV}$", CMS Physics Analysis Summary CMS-PAS-LUM-18-002, CERN, Geneva, 2019.

[39] T. Sjöstrand et al., "An introduction to PYTHIA 8.2", *Comput. Phys. Commun.* **191** (2015) 159, doi:10.1016/j.cpc.2015.01.024, arXiv:1410.3012.

[40] CMS Collaboration, "Event generator tunes obtained from underlying event and multiparton scattering measurements", *Eur. Phys. J. C* **76** (2016) 155, doi:10.1140/epjc/s10052-016-3988-x, arXiv:1512.00815.

[41] CMS Collaboration, "Extraction and validation of a new set of CMS PYTHIA8 tunes from underlying-event measurements", *Eur. Phys. J. C* **80** (2019) 4, doi:10.1140/epjc/s10052-019-7499-4, arXiv:1903.12179.

[42] J. Alwall et al., "The automated computation of tree-level and next-to-leading order differential cross sections, and their matching to parton shower simulations", *JHEP* **07** (2014) 079, doi:10.1007/JHEP07(2014)079, arXiv:1405.0301.

[43] S. Alioli et al., "Jet pair production in POWHEG", *JHEP* **04** (2011) 081, doi:10.1007/JHEP04(2011)081, arXiv:1012.3380.

[44] S. Frixione, P. Nason, and C. Oleari, "Matching NLO QCD computations with parton shower simulations: the POWHEG method", *JHEP* **11** (2007) 070, doi:10.1088/1126-6708/2007/11/070, arXiv:0709.2092.

[45] P. Nason, "A new method for combining NLO QCD with shower Monte Carlo algorithms", *JHEP* **11** (2004) 040, doi:10.1088/1126-6708/2004/11/040, arXiv:hep-ph/0409146.

[46] GEANT4 Collaboration, "GEANT4—a simulation toolkit", *Nucl. Instrum. Meth. A* **506** (2003) 250, doi:10.1016/S0168-9002(03)01368-8.

[47] CMS and TOTEM Collaborations, "Proton reconstruction with the Precision Proton Spectrometer in Run 2", 2022. arXiv:2210.05854. Submitted to JINST.

[48] D. Krohn, J. Thaler, and L.-T. Wang, "Jet trimming", *JHEP* **02** (2010) 084, doi:10.1007/JHEP02(2010)084, arXiv:0912.1342.

[49] CMS Collaboration, "A multi-dimensional search for new heavy resonances decaying to boosted WW, WZ, or ZZ boson pairs in the dijet final state at 13 TeV", *Eur. Phys. J. C* **80** (2020) 237, doi:10.1140/epjc/s10052-020-7773-5, arXiv:1906.05977.

[50] CMS Collaboration, "Technical proposal for the Phase-II upgrade of the Compact Muon Solenoid", CMS Technical Proposal CERN-LHCC-2015-010, CMS-TDR-15-02, 2015.

[51] CMS Collaboration, "Particle-flow reconstruction and global event description with the CMS detector", *JINST* **12** (2017) P10003, doi:10.1088/1748-0221/12/10/P10003, arXiv:1706.04965.

[52] M. Cacciari, G. P. Salam, and G. Soyez, "The anti-k_{T} jet clustering algorithm", *JHEP* **04** (2008) 063, doi:10.1088/1126-6708/2008/04/063, arXiv:0802.1189.

[53] M. Cacciari, G. P. Salam, and G. Soyez, "FastJet user manual", *Eur. Phys. J. C* **72** (2012) 1896, doi:10.1140/epjc/s10052-012-1896-2, arXiv:1111.6097.

[54] CMS Collaboration, "Jet energy scale and resolution in the CMS experiment in pp collisions at 8 TeV", *JINST* **12** (2017) P02014, doi:10.1088/1748-0221/12/02/P02014, arXiv:1607.03663.

[55] J. Thaler and K. Van Tilburg, "Identifying boosted objects with N-subjettiness", *JHEP* **03** (2011) 015, doi:10.1007/JHEP03(2011)015, arXiv:1011.2268.

[56] S. D. Ellis, C. K. Vermilion, and J. R. Walsh, "Recombination algorithms and jet substructure: pruning as a tool for heavy particle searches", *Phys. Rev. D* **81** (2010) 094023, doi:10.1103/PhysRevD.81.094023, arXiv:0912.0033.

[57] CMS Collaboration, "Identification techniques for highly boosted W bosons that decay into hadrons", *JHEP* **12** (2014) 017, doi:10.1007/JHEP12(2014)017, arXiv:1410.4227.

[58] J. Dolen et al., "Thinking outside the ROCs: designing decorrelated taggers (DDT) for jet substructure", *JHEP* **05** (2016) 156, doi:10.1007/JHEP05(2016)156, arXiv:1603.00027.

[59] F. Nemes, "LHC optics determination with proton tracks measured in the CT-PPS detectors in 2016, before TS2", Technical Report CERN-TOTEM-NOTE-2017-002, 2017.

[60] J. Kašpar, "Alignment of CT-PPS detectors in 2016, before TS2", Technical Report CERN-TOTEM-NOTE-2017-001, 2017.

[61] L. Harland-Lang, V. Khoze, and M. G. Ryskin, "Elastic photon-initiated production at the LHC: the role of hadron-hadron interactions", *SciPost Physics* **11** (Sep, 2021) 064, doi:10.21468/scipostphys.11.3.064, arXiv:2104.13392.

[62] J. S. Conway, "Incorporating nuisance parameters in likelihoods for multisource spectra", in *PHYSTAT 2011*, p. 115. 2011. arXiv:1103.0354. doi:10.5170/CERN-2011-006.115.

[63] CMS Collaboration, "Search for WWγ and WZγ production and constraints on anomalous quartic gauge couplings in pp collisions at $\sqrt{s} = 8$ TeV", *Phys. Rev. D* **90** (2014) 032008, doi:10.1103/PhysRevD.90.032008, arXiv:1404.4619.

[64] HEPData record for this analysis, 2022. doi:10.17182/hepdata.135991.